Catalysis Letters (2024) 154:155–169
https://doi.org/10.1007/s10562-023-04285-3

Catalytic Oxidation of Propane and Carbon Monoxide by Pd Nanoparticles on Mn/TiO_2 Catalysts

Roberto Camposeco[1] · Salvador Castillo[2] · Rodolfo Zanella[1]

Received: 8 December 2022 / Accepted: 18 January 2023 / Published online: 7 February 2023

Abstract

The present work shows experimental results on the catalytic oxidation of C_3H_8 and CO by Pd nanoparticles supported on MnO_x/TiO_2 synthesized by the sol–gel method. The results show a strong interaction between Pd and MnO_x/TiO_2; likewise, the annealing temperature of the TiO_2 support modified the catalytic properties of the Pd–MnO_x/TiO_2 catalyst. In this line, the catalysts with 1 and 2 wt% of Pd loading supported on MnO_x/TiO_2 showed outstanding catalytic activity oxidizing C_3H_8 and CO within two temperature intervals: 200–400 °C and 25–200 °C, respectively. The Pd–MnO_x/TiO_2 catalyst also displayed very high stability during long-term tests and the addition of Pd nanoparticles reduced greatly the oxidation temperature of MnO_x/TiO_2. The outcomes revealed that the Pd–Mn interaction promoted the formation of new Pd^0/Pd^{2+} active sites as well as the formation of oxygen vacancies and reduced Ti^{4+} to Ti^{3+} species, which led to the improvement of the Mn^{3+} and Mn^{4+} redox features, thus boosting the catalytic oxidation capacity of the Pd–MnO_x/TiO_2 catalyst.

Graphical Abstract

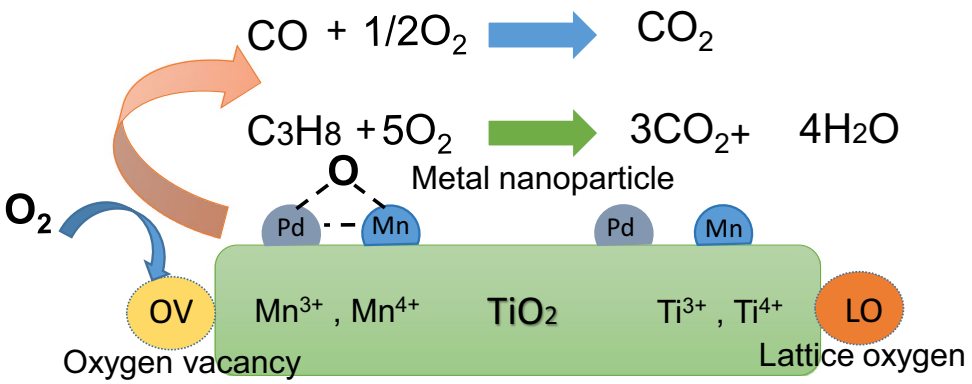

Keywords Oxidation · Propane · Carbon monoxide · Palladium · Nanostructures

1 Introduction

The catalytic oxidation of propane and carbon monoxide have important applications in various areas and industrial sectors to control pollution in urban areas generated by both stationary and mobile sources [1]. In both cases, the main technology employed to reduce the production of contaminating compounds that are released into the atmosphere and comply with the strict emission limits of environmental regulations is the use of catalytic systems [2, 3].

✉ Rodolfo Zanella
rodolfo.zanella@icat.unam.mx

[1] Instituto de Ciencias Aplicadas y Tecnología, Universidad Nacional Autónoma de México, Circuito Exterior S/N, C. U., 04510 Mexico City, Mexico

[2] Dirección de Tecnología del Producto, Instituto Mexicano del Petróleo, Eje Central Lázaro Cárdenas 152, San Bartolo Atepehuacan, Gustavo A. Madero, 07730 Mexico City, Mexico

In the automotive sector, the most important technological measure put into practice to reduce the emissions generated by gasoline vehicles was the introduction of the three-way catalytic converter. In this sense, catalytic systems of this type containing supported Pd represent a real alternative due to their excellent catalytic activity in the oxidation of carbon monoxide and hydrocarbons (HCs) at low temperature compared to those containing supported Pt and Rh [4, 5]. However, the main challenges for the use of palladium in the three-way catalytic converter are related to poisoning, sintering, and selectivity of HCs to CO_2, avoiding the formation of CO, in addition to some difficulties to carry out the NO_x reduction [4, 5, 10].

Recently, to replace noble metals in oxidation catalysts, more attention has been paid to the study of hydrotalcites, spinels, perovskites, and single-oxide catalysts like cobalt, copper, iron, manganese, or nickel [4, 6–9]. In the case of stationary sources, the technology has been focused mainly on the selective catalytic reduction (SCR-NO_x) [10]. This technology uses CO generated during the combustion process and partially burned hydrocarbons as well as the addition of NH_3 as NO_x reducing agents [11]. In all cases, it has been reported [12] that the support used to a greater extent is TiO_2. Currently, there are several TiO_2 synthesis routes like the sol–gel method, [13] controlled precipitation, [14] and hydrothermal synthesis as the main ones [15]. Likewise, there are several methodologies for the deposition or impregnation of active metals on TiO_2, from which the wet impregnation and chemical precipitation stand out [16] Furthermore, the addition of noble metals reduces considerably the operating temperature window, improving the total oxidation of hydrocarbons [17]. These compounds are undesirable in the environment, because CO negatively affects the health of the population, while hydrocarbons react in the atmosphere with NO_x in the presence of sunlight to form ozone [18, 19].

For total oxidation catalytic reactions, noble metals such as Au, Pt, Pd and Ru supported on an oxide with high surface area have been employed [20]. Pt and Pd are known for their excellent activity for many reactions, including C_3H_8 and CO oxidation, due to their resistance to poisoning and tolerance to moisture [21]. Notwithstanding, in recent studies, loss of catalytic activity for C_3H_8 oxidation has been reported for Pd/Al_2O_3, which has been related to sintering and reducibility of the PdO_x active sites and generation of metallic Pd [22]. The low temperature C_3H_8 oxidation has been investigated employing platinum catalysts on different supports (MgO, La_2O_3, Al_2O_3, ZrO_2, SiO_2, SiO_2–Al_2O_3 and SO_4^{2-}–ZrO_2), and the best results were given by Pt/Al_2O_3–SiO_2 mixed oxide [23]. It is worth mentioning that propane has been used as a model hydrocarbon molecule because it is very stable and as consequence, difficult to oxidize, and in the presence of heat or light, the reaction involves the breaking of C–H and C–C bonds [23–25]. On the other hand, the development of bimetallic catalysts is considered as a promising alternative in terms of stability and high activity with regard to monometallic catalysts for C_3H_8 and CO oxidation; for example, the AuPd nanoalloy supported on a Mo(110) substrate has shown high catalytic activity and improved stability toward the C_3H_8 oxidation [24].

Regarding the support, the reducible ones such as TiO_2 and CeO_2 have exhibited significant positive effects on the catalytic activity of Pd, Pt, Rh, PdRh metal nanoparticles during the C_3H_8 oxidation due to their ability to provide reactive oxygen [25]. However, to achieve better catalytic activity, it is necessary to improve the ability of the oxide to provide reactive oxygen, mainly in the case of TiO_2. One way to increase the oxygen ability on TiO_2 is by forming oxygen vacancies to increase the reduction of Ti^{4+} to Ti^{3+} species, which can be achieved through the synthesis of mixed oxides such as MnO_x–TiO_2, which can also improve the Mn redox features.

At the same time, mixed oxides have shown to be promising for the C_3H_8 oxidation; for example, Pt/V_2O_5/Al_2O_3, Pd/V_2O_5–Al_2O_3 and Pd/WO_x/TiO_2 catalysts have displayed an increase in the acidity, better metal dispersion and the production of highly reactive oxygen that improve the catalytic activity [26–28]. Besides, for the C_3H_8 and CO oxidation, some transition metal oxides such as MnO_2 and Co_3O_4 have had similar activity to that displayed by noble metals [29–31]. Also, it has been reported previously that the acid/base strength of the support affects the catalytic performance of the C_3H_8 oxidation in terms of dispersion and oxidation state of supported Pd or Pt [23].

Regarding Pd catalysts supported on MnO_x/TiO_2, a few research works have reported their use, showing synergism between Pd–Mn and good palladium dispersion in the total oxidation of acetone and CO_2 reduction in ethanol, [18, 32] however, to the best of our knowledge the Pd–MnO_x/TiO_2 has not been studied as catalyst for the propane oxidation.

Based on the previous background, the aim of the present work was to study the effect of the interaction between Pd nanoparticles and MnO_x supported on TiO_2 with moderate surface area, obtained by the sol–gel method, on the catalytic activity for the C_3H_8 and CO oxidation reactions. The catalytic activity was highlighted as a function of the reaction temperature, correlating the conversion of propane and carbon monoxide with the content and dispersion of Pd, oxygen vacancies as well as reduced Ti^{3+}, Mn^{4+} and Mn^{3+} species by X-ray photoelectron spectroscopy in order to contribute to the understanding of the performance of the ternary Pd–MnO_x/TiO_2 system in these oxidation reactions.

2 Experimental Section

For the synthesis of TiO_2 by the sol–gel method, titanium isopropoxide was used as a precursor (99.99% Aldrich). The employed solvent was 2-propanol with a 2-propanol:titanium isopropoxide ratio of 6:1. The mixture was brought to room temperature to then apply heating until reaching 70 °C under constant stirring. Then, nitrate tetrahydrate ($MnN_2O_6{\cdot}4H_2O$, Aldrich 97%) was used to obtain a loading of 6 wt% of manganese by adding it dropwise to a solution of 2-propanol, water, and HNO_3. The catalysts synthesized via sol–gel were calcined at 500 and 700 °C for 4 h in a flow of 80 mL/min of air. As for palladium nanoparticles, they were obtained by the deposition–precipitation with urea (DPU) method. The palladium theoretical loadings were 1 and 2 wt%. Palladium (II) chloride (Sigma-Aldrich, 99.9%) and urea were dissolved in 25 mL of distilled water. Then, 500 mg of MnO_x/TiO_2 were added to this solution under constant stirring; thereafter, the suspension temperature was increased up to 80 °C and kept at constant stirring for 16 h. After the DPU procedure, all the samples were centrifuged, washed with water at 50 °C and then centrifuged four times and dried under vacuum for 2 h at 80 °C, and then they were treated at 500 °C for 4 h in a flow of 80 mL/min of air. The pretreated catalysts were labeled as $Pd–MnO_x/TiO_2$.

2.1 Catalytic Tests

2.1.1 Propane Oxidation Test

For the catalytic activity tests, 80 mg of catalyst were used. The catalyst samples were placed in a tubular quartz reactor (ID = 1 cm) mounted in an electric oven that allows heating at a programmed temperature, using a RIG 150 device from in-situ research. A porous quartz frit was placed in the middle of the tube that supported the catalyst. Prior to catalytic tests, the samples were calcined in-situ at 500 °C for 4 h in a flow of 80 mL/min of air. The heating ramp was 3 °C per min. After heating, the sample was cooled down to room temperature in the same gas flow. Flow mass controllers were used to set the flow of a gas mixture containing 5000 ppm of C_3H_8 and 2% O_2 balanced with N_2. The total flow was 100 mL/min. The space velocity, defined as the ratio of the volume of the catalyst to the total flow of reaction gas was around 44,000 h^{-1}. CO_2 concentrations in the effluent gas were monitored online using a gas chromatograph Agilent Technologies 6890 network GC system equipped with a methanizer. During the catalytic tests, the reactor temperature was raised from room temperature to 600 °C at a rate of 3 °C per min. Propane conversion (%) = $([C_3H_8]_{in} - [C_3H_8]_{out}/[C_3H_8]_{in}) \times 100$.

2.1.2 CO Oxidation Test

The CO oxidation reaction was studied in a flow reactor at atmospheric pressure by increasing the temperature from RT to 400 °C (light off test). 40 mg of dried catalyst were first activated in-situ with a flow of 40 mL/min of air at a heating rate of 3 °C/min up to the final chosen temperature. The reactant gas mixture (1 vol% CO and 1 vol% O_2 balanced with N_2) was introduced with a total flow rate of 100 mL/min, and a heating rate of 3 °C/min. The gases were analyzed with an Agilent Technologies 6890N online gas chromatograph equipped with a FID detector, a methanizer and an HP Plot Q column. The stability of the catalysts versus time on stream was examined at 20 °C for a 20-h run, using 40 mg of catalyst activated in-situ in air using the same heating rate. CO conversion (%) = $([CO]_{in} - [CO]_{out}/[CO]_{in}) \times 100$.

Dispersion (D), which is defined as the fraction of metal atoms located at the surface of the particle with regard to the total amount of metal atoms of the particle, taking into account a spherical particle, was calculated using the following Eq. (1):

$$D = \frac{6M}{D_p \rho \sigma N_A} \tag{1}$$

where D is the metal fractional dispersion, M is the molecular weight of the metal (g/mol), D_p is the metal particle size, ρ is the metal density (g/cm^3), σ is the area occupied by a surface metal atom (A^2/atom), and N_A is Avogadro's constant.

The turnover frequency (TOF) was calculated using the dispersion (D) and Eq. (2):

$$TOF = \frac{R * M}{D} \tag{2}$$

where R is the rate (mol/g*Pd/s), D is the metal fractional dispersion and M is the molecular weight of the metal (g/mol). Likewise, the activation energy E_a was calculated using Arrhenius Eq. (3):

$$lnk = lnA - \frac{Ea}{RT} \tag{3}$$

where k is the rate constant, E_a is the activation energy, R is the gas constant, T is the reaction temperature and A is the frequency factor constant also known as pre-exponential factor.

2.2 Characterization of the Catalysts

X-ray diffraction (XRD) patterns were recorded at room temperature with Cu Kα radiation in a Bruker Advance

D-8 diffractometer having a theta–theta configuration and a graphite secondary-beam monochromator. The data were collected for scattering angles (2θ) ranging from 4° to 80° with a step size of 0.02° for 2 s per point. High resolution transmission electron microscopy (HRTEM) analyses of the samples were performed with a JEOL 2200FS microscope operating at 200 kV and equipped with a Schottky-type field emission gun and ultrahigh resolution pole piece (Cs = 0.5 mm, point-to-point resolution, 0.190 nm). The textural properties were obtained by means of an ASAP-2000 analyzer from Micromeritics. The specific surface area S_{BET} was calculated from the Brunauer–Emmett–Teller (BET) equation from N_2 physisorption at 77 K. The hydrogen temperature programmed reduction study of the photocatalysts was obtained in a RIG-150 TPR analyzer unit under a flow of 10% H_2/Ar gas mixture (20 mL/min) with a heating rate of 10 °C/min from room temperature to 600 °C. Before starting the heating process, a flow of 25 mL/min of 10% H_2/Ar gas mixture was passed through the sample to stabilize the TCD signal. Diffuse Reflection Infrared Fourier Transform Spectroscopy (in-situ DRIFTS) was collected in a Nicolet 8700 spectrophotometer equipped with a Praying Mantis diffuse reflection cell and high-temperature reaction chamber by Harrick. In each experiment, approximately 25–30 mg of sample were packed in the sample holder and pretreated in situ under air flow (30 mL/min, heating rate of 2 °C/min) up to the chosen temperature. After the thermal treatment, the sample was cooled down to room temperature under the same gas flow and then purged with N_2 before the introduction of 5% of CO in N_2 (30 mL/min). A spectrum registered under N_2 was used as reference; then, several spectra were recorded under CO flow until the band intensity was stable; afterwards, the temperature was increased under CO and spectra were obtained at different increasing temperatures. The XPS analyses were performed with a Thermo VG Scientific Escalab 250 spectrometer equipped with a hemispherical electron analyzer and an Al Kα radiation source (1486.6 eV) powered at 20 kV and 30 mA. The binding energy was determined by using carbon C (1s) as reference line (284.6 eV). The spectrometer was operated at pass energy of 23.5 eV, and the base pressure in the analysis chamber was maintained in the order of 3×10^{-8} mbar. Peak fitting was done by using XPSPEAK 41 with Shirley background.

3 Results and Discussion

3.1 Crystalline and Textural Properties

X-Ray diffraction (XRD) patterns are displayed in Fig. 1A and B for the TiO_2, 2Pd/TiO_2, 6MnO_x/TiO_2, 1Pd–MnO_x/TiO_2 and 2Pd–MnO_x/TiO_2 catalysts annealed at 500 °C,

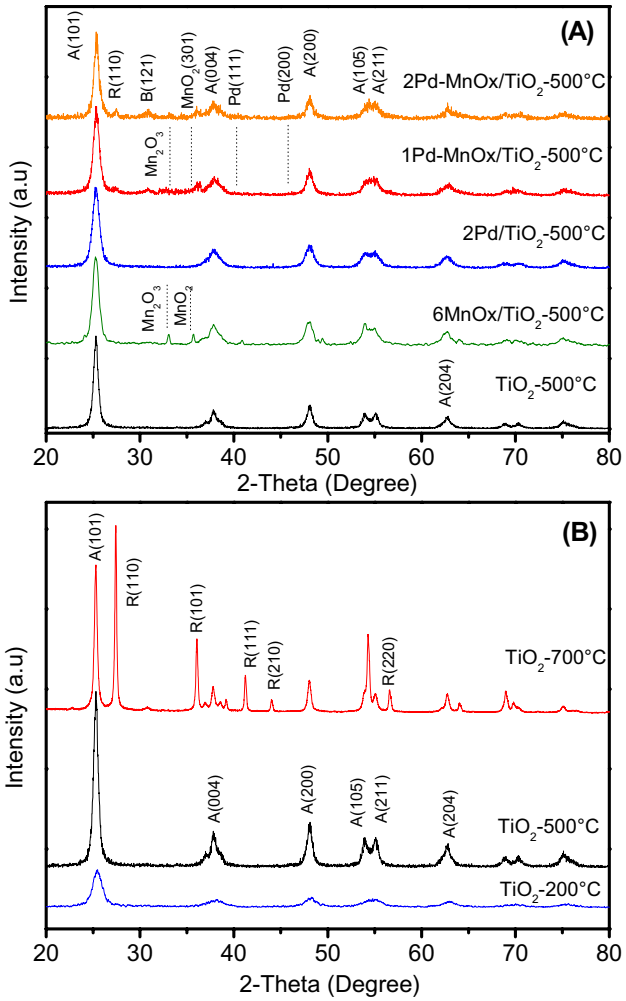

Fig. 1 **A** X-ray diffraction patterns of the TiO_2-500 °C, 2Pd/TiO_2, 6MnO_x/TiO_2, 1Pd–MnO_x/TiO_2 and 2Pd–MnO_x/TiO_2 catalysts annealed at 500 °C, **B** X-ray diffraction patterns of TiO_2-200, TiO_2-500 and TiO_2-700, where A, B and R refer to the anatase, brookite and rutile phases

where it is observed that all of them contain anatase as the main phase, showing peaks at 2θ = 25.3° (101), 37.8° (004), 48.1° (200), and 55.1° (211) in agreement with the JCPDS 21–1272 card. In addition, slight peaks associated with the brookite and rutile phases at 2θ = 30.80° (211), and 2θ = 27.44° (110), according to the JPDCS 75-1582 and JPDCS 75-1582 cards, respectively, can be observed mainly for the 2Pd–MnO_x/TiO_2 catalyst. Earlier studies have shown that the deposition of different metals such as Cu, Cr, Co, Na, Ni, Sn, Al and Zn on TiO_2 promoted the emergence of the rutile phase at high temperatures [23, 33]. In the XRD patterns of the 1Pd–MnO_x/TiO_2 and 2Pd–MnO_x/TiO_2 catalysts, the presence of small peaks that can be assigned to Mn_3O_4 and MnO_2 species is noted. Previous studies showed that the MnO_x phases were not identified at low concentrations in TiO_2, while they were plainly detected when the

quantity of Mn was above 15 wt% [34]. Additionally, palladium peaks at 2θ = 40.11° (111) and 46.65° (200) are not observed in both the 1- and 2-wt.% samples, according to the JPDCS 46-1043 card, since high dispersions and low palladium contents might escape the XRD detection.

Furthermore, the X-ray diffraction patterns of the TiO_2 support calcined at 200, 500 and 700 °C are shown in Fig. 1B, where the anatase phase prevails with the presence of higher intensity peaks assigned to the rutile phase (110) mainly at 700 °C. At the annealing temperature of 500 °C, it is observed that the peak width of the anatase (101) plane, located at 2θ = 25.3°, is wider than that of the sample treated at 700 °C; another effect observed when the temperature was increased up to 700 °C was that the intensity of the anatase plane, 2θ = 25.3° (101), grew and became more cramped; hence, the crystallite size also increased. In this context, a higher annealing temperature (700 °C) disclosed intensified presence of the rutile phase, which was due to the transition from the anatase to rutile phase caused by the temperature increase [35]. Regarding the N_2 adsorption, the outcomes revealed that the addition of palladium and manganese to the TiO_2 support treated at 500 °C did not cause changes in the BET surface area despite the addition of metal loadings of 1, 2 and 6 wt%. The surface area values were around 91–107 m^2/g, see Table 1. Also, N_2 adsorption–desorption isotherms provided information about the surface area, pore volume and pore size distribution for the TiO_2-500, 2Pd/TiO_2-500, 6MnO_x/TiO_2, 1Pd–MnO_x/TiO_2 and 2Pd–MnO_x/TiO_2 catalysts annealed at 500 and 700 °C, see Fig. 2. The isotherms of the TiO_2-500, 2Pd/TiO_2-500, 6MnO_x/TiO_2, 1Pd–MnO_x/TiO_2 and 2Pd–MnO_x/TiO_2 catalysts are representative of mesoporous materials and show type IV isotherms and H2 hysteresis loop (IUPAC classification) [36], see Fig. 2. With respect to the TiO_2 catalyst treated at 700 °C, the specific area decreased drastically to 18 m^2/g.

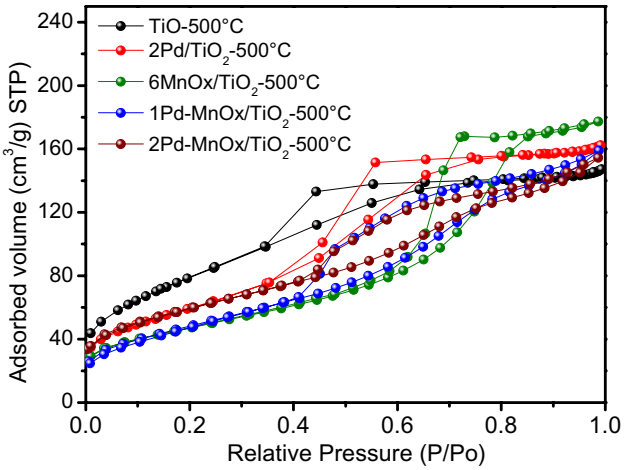

Fig. 2 N_2 adsorption–desorption isotherms for the 2Pd/TiO_2, 6MnO_x/TiO_2, 1Pd–MnO_x/TiO_2 and 2Pd–MnO_x/TiO_2 catalysts annealed at 500 °C

3.2 Particle Size Determined by HRTEM

Figure 3A and B display HRTEM micrographs as well as the corresponding size distribution of palladium nanoparticles in the 2Pd/TiO_2 and 2Pd–MnO_x/TiO_2 catalysts annealed at 500 °C. Semi-spherical palladium nanoparticles are observed dispersed homogeneously on the TiO_2 support and 6MnO_x/TiO_2 with an average size around 2.4 and 2.6 nm, see Fig. 3 and Table 1. As for the measuring of the lattice space of fringes through HRTEM, the exposed plane of Mn oxide species was Mn_2O_3 (321) with $d = 0.25$ nm. Also, in the HRTEM images of the 2Pd/TiO_2 and 2Pd–MnO_x/TiO_2 catalysts, the (111) plane of palladium was found showing a lattice fringe of 0.22 nm located around the TiO_2 and MnO_x interface. Likewise, Fig. 3C shows a TEM image of the 6MnO_x/TiO_2 sample annealed at 500 °C and the analysis of the EDS spectra confirmed the presence of manganese and titanium oxides.

3.3 Reducibility of Palladium and Manganese Species (H_2/TPR)

Temperature programmed reduction by hydrogen (H_2/TPR) was used to observe the behavior of the reducible species of manganese and palladium loaded on TiO_2. The

Table 1 Physicochemical characteristics and catalytic performance of the synthesized samples

Catalysts	S_{BET} (m^2/g)	Pd Particle Size (nm)	Rate $_{C3H8\ Ox}$ mol/(g_{cat}·s)*	Rate $_{CO\ Ox}$ mol/(g_{cat}·s)**	$E_{a\ C3H8}$ (kJ/mol)	$E_{a\ CO}$ (kJ/mol)	TOF $_{CO}$ (s^{-1})	TOF $_{C3H8}$ (s^{-1})	Pd Dispersion (%)
TiO_2-500 °C	107	–	5.1×10^{-8}	4.12×10^{-5}	–	–	–	–	–
TiO_2-700 °C	18	–	2.8×10^{-8}	–	–	–	–	–	–
2Pd/TiO_2-500 °C	97	2.4	1.7×10^{-7}	3.91×10^{-4}	90.2	48.8	0.010	4.4×10^{-4}	41
6MnO_x/TiO_2-500 °C	92	–	3.8×10^{-7}	3.97×10^{-4}	91.4	49.4	–	–	–
1PdMnO_x/TiO_2-500 °C	101	–	2.1×10^{-6}	2.82×10^{-3}	–	43.6	0.055	5.7×10^{-3}	37
2PdMnO_x/TiO_2-500 °C	97	2.6	3.1×10^{-6}	2.03×10^{-3}	78	42.2	0.077	8.4×10^{-3}	39

*The C_3H_8 oxidation rate was determined at 300 °C, ** the CO oxidation rate was determined at 100 °C

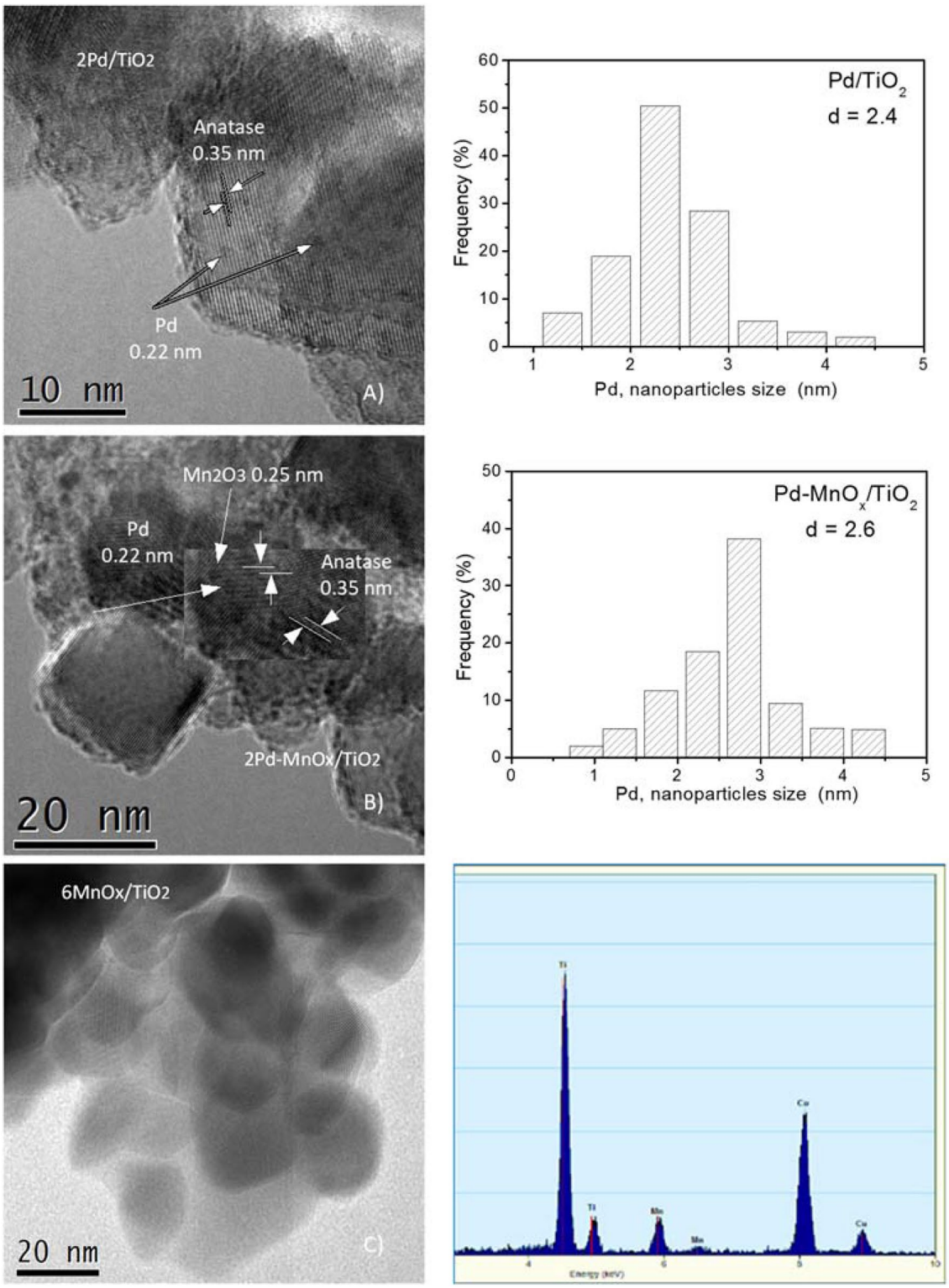

Fig. 3 HRTEM micrographs of the samples annealed at 500 °C **A** 2Pd/TiO_2 and crystal size frequency histogram; **B** 2Pd–MnO_x/TiO_2 and crystal size frequency histogram; and **C** 6MnO_x/TiO_2 and EDS analysis of the sample

profiles of the $2Pd/TiO_2$, $6MnO_x/TiO_2$, $1Pd–MnO_x/TiO_2$ and $2Pd–MnO_x/TiO_2$ catalysts are shown in Fig. 4. The peaks located between 200 and 400 °C are ascribed to the reduction of MnO_2 to Mn_2O_3 to Mn_3O_4, and Mn_3O_4 to Mn^0 species [37]. The prominent peak located at 400 °C for the $6MnO_x/TiO_2$ catalyst, and at 300 °C for the $1Pd–MnO_x/TiO_2$ and $2Pd–MnO_x/TiO_2$ catalysts, indicates that MnO_2 and Mn_2O_3 are the dominant phases in all of them. These results reveal that Mn was found as Mn^{4+} and Mn^{3+} in TiO_2. No clear reduction peak related to PdO_x species was observed for the $2Pd/TiO_2$, $1Pd–MnO_x/TiO_2$ and $2Pd–MnO_x/TiO_2$ catalysts, which can be due to the reduction of this oxide during the stabilization of the TCD signal (at room temperature) as soon as hydrogen and palladium came into contact, at the beginning of the analysis, as a consequence of the easiness of that process in this kind of catalysts. As for the negative peaks located at around 92 and 94 °C, they are related to the release of hydrogen due to the adsorption and dissociation of the palladium–hydrogen bond formation ($Pd–H_x$). Palladium in the form of nanoparticles is capable of absorbing hydrogen to form Pd hydride at room temperature, as shown by the $2Pd/TiO_2$, $1Pd–MnO_x/TiO_2$ and $2Pd–MnO_x/TiO_2$ catalysts (Fig. 4), which is in agreement with [13, 38]. Moreover, previous studies have reported that the reduction of PdO takes place at 19 °C followed by the adsorption-dissociation of palladium–hydrogen bond formation ($Pd–H_x$) [39]. In this sense, in a previous work on the role played by Pd b-hydride catalysts in the reduction of nitrate, the authors prepared two catalysts using different palladium precursors: the first one was $Pd(C_5H_7O_2)_2$ (99%) in toluene, and the second one was an aqueous solution of $Pd(NO_3)_2$ (99%). The TPR analysis of these samples showed a negative peak, which became more noticeable when the palladium acetyl

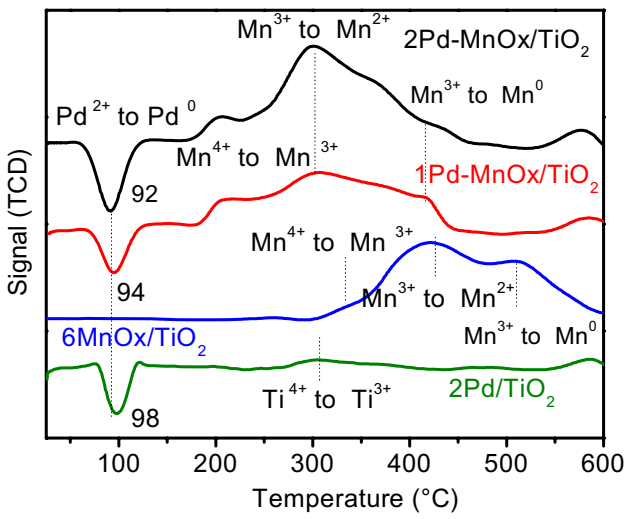

Fig. 4 TPR profiles for the $2Pd/TiO_2$, $6MnO_x/TiO_2$, $1Pd–MnO_x/TiO_2$ and $2PdMnO_x/TiO_2$ catalysts

acetonate precursor was used than when palladium nitrate was employed, where reduction occurred at 75 and 45 °C, respectively. The authors showed that this peculiar behavior was due to hydrogen that evolved during the decomposition of the hydride phase, considering that palladium absorbs hydrogen to form Pd hydride even at low hydrogen pressures and room temperatures; the authors reported metal sizes of 2 and 10 nm, showing a more defined and negative peak when the palladium particle size was 10 nm. As far as our study is concerned, palladium (II) chloride (Sigma-Aldrich, 99.9%) was used as a palladium precursor, showing a negative peak between 94 and 98 °C with palladium particle sizes of 2.4 and 2.6 nm, which seems to be in good agreement with the tendency reported in previous studies, showing that the formation of the hydride phase decreases with the increase in the Pd dispersion in supported catalysts, even when the palladium precursor is different [40–42]. On the other hand, according to TPR profiles, the PdO_x reduction peak overlapped the TiO_2 reduction peak at 320 °C, which is in agreement with a previous study [43]. Earlier studies have described that the negative reduction peak is a common feature in Pd-based catalysts [44]. The adsorption of H_2 was carried out on the surface of the $2Pd/TiO_2$ catalyst at low temperatures and hydrogen was released in the form of H_2 when the temperature was elevated above 90 °C, as seen in Fig. 4. With the addition of palladium to MnO_x/TiO_2, the reduction peaks of Mn show a displacement to lower temperatures. The outcomes disclosed that the palladium catalysts generated a strong surface contribution, interacting with MnO_x and as consequence, the reduction temperature decreased. This diminution in the reduction temperature of manganese could be due to the presence of surface oxygen vacancies in the $1Pd–MnO_x/TiO_2$ and $2Pd–MnO_x/TiO_2$ catalysts because of the interaction between the palladium nanoparticles and MnO_x/TiO_2, which promoted the reducibility of the manganese nanoparticles at lower temperatures. Each $2Pd/TiO_2$, $1Pd–MnO_x/TiO_2$ and $2Pd–MnO_x/TiO_2$ catalyst showed a different intensity in this negative and broad peak related to PdH_x between 50 and 150 °C, where the intensity was the lowest for $1Pd–MnO_x/TiO_2$ and slightly higher for $2Pd–MnO_x/TiO_2$ catalysts, suggesting the presence of small Pd particles. The Pd/TiO_2 catalyst exhibited positive peak regions at approximately 320 and 580 °C, respectively. These positive peaks indicated that bulk PdO_x species were reduced to PdO or may be related to hydrogen spillover from the metal catalyst surface [39]. If a full Pd reduction is considered ($Pd^{2+} \leftrightarrow Pd^0$), the possible reduction reaction that might take place during the TPR is: $PdO + H_2 \rightarrow Pd^0 + H_2O$. The stoichiometric amount of H_2 is 1 mol H_2/mol of PdO, or $H_2/Pd = 1$. The samples show an increase in the H_2 consumption as the palladium charge increases, with values of 140 μmol H_2 g^{-1} for $2Pd/TiO_2$, 128 μmol H_2 g^{-1} for $1Pd–MnO_x/TiO_2$ and of 235 μmol H_2 g^{-1} for $2Pd–MnO_x/$

TiO_2, respectively. The experimental estimation for 2 wt% of Pd is 195 µmol H_2 g^{-1}, also suggesting some co-reduction of palladium at the TiO_2 and Mn/TiO_2 catalyst interphase.

3.4 Surface Evolution by XPS

X-ray photoelectron spectroscopy (XPS) outcomes for titanium 2p, manganese 2p, palladium 3d as well as oxygen 1s, and the deconvolution of spectra performed for the $2Pd/TiO_2$, $6MnO_x/TiO_2$, and $2Pd–MnO_x/TiO_2$ catalysts are shown in Fig. 5. The spectrum deconvolution for the $2Pd/TiO_2$ and $2Pd–MnO_x/TiO_2$ catalysts indicates that the Pd species are found in two different states, mainly as Pd^{2+} and Pd^0 species. Figure 5 displays results in terms of the main binding energies (BEs); likewise, the surface states of palladium were obtained by the deconvolution of Pd 3d peaks for the palladium catalysts. Mostly, the amount of metallic Pd^0 and Pd^{2+} for the $2Pd/TiO_2$ and $2Pd–MnO_x/TiO_2$ catalysts is balanced, see Table 2. Furthermore, an additional peak is observed in the $2Pd–MnO_x/TiO_2$ catalyst, which is attributed to Ti–O–Pd species due to the fact that the lattice oxygen 1s and reduced Ti^{3+} increased notably. Earlier studies have reported that a higher proportion of oxygen defects could be obtained on the Pd/TiO_2 catalysts with respect to bare TiO_2, which facilitates the electron transfer from TiO_{2-x} to metallic Pd, [45] leading to electron enrichment on the Pd particles. The resulting O_2 adsorption on Pd could be enhanced through back donation of electrons from Pd species to the antibonding π* orbital of O_2 [46].

Figure 5 displays the Ti 2p XPS spectra for the $6MnO_x/TiO_2$, $2Pd–MnO_x/TiO_2$ and $2Pd/TiO_2$ catalysts, which consist of two peaks that have to do with Ti $2p_{1/2}$:456.5 eV and

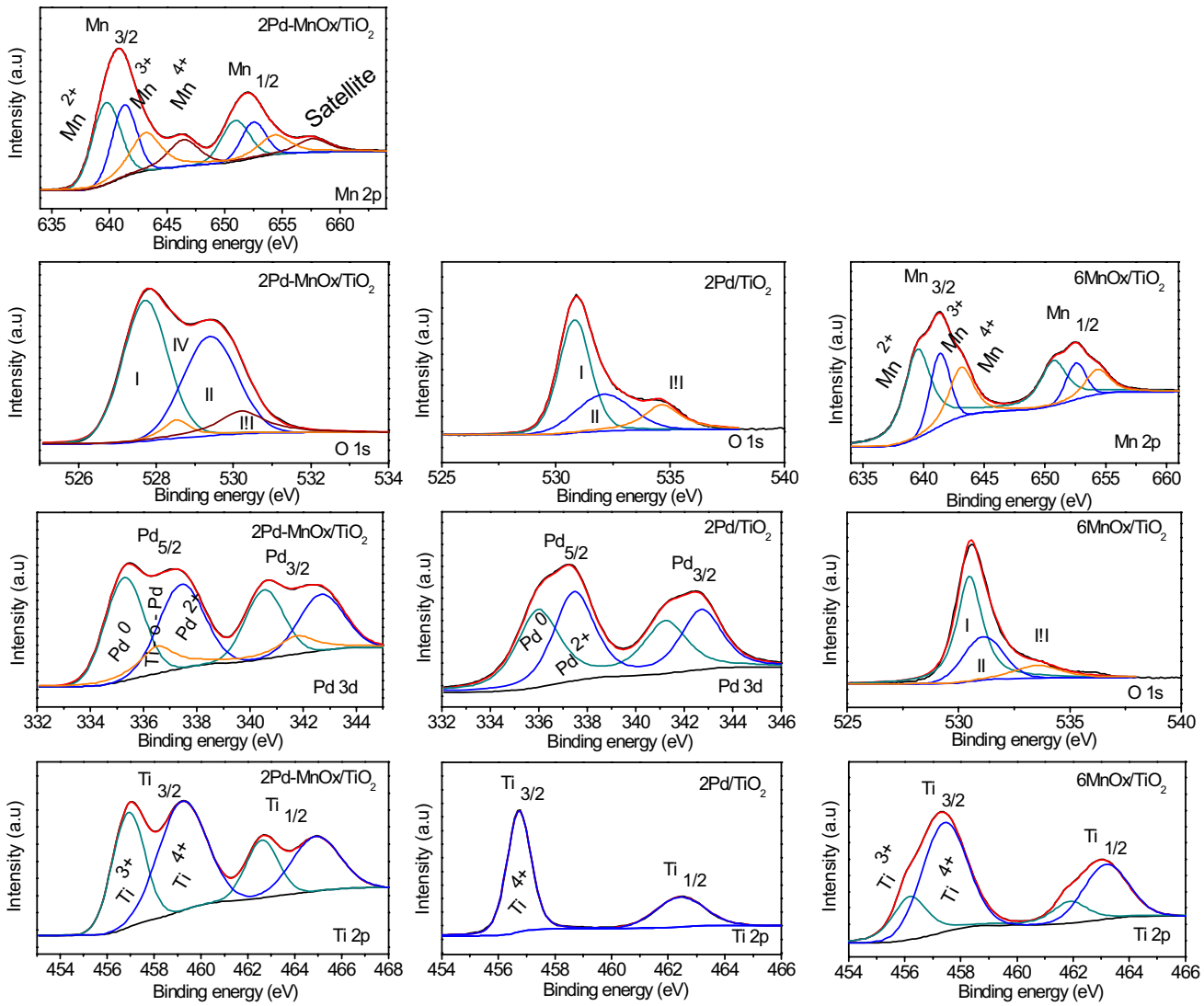

Fig. 5 X-ray photoelectron spectroscopy spectra over O 1s, Ti 2p, Pd 3d, and Mn 2p peaks for the $2Pd/TiO_2$, $6MnO_x/TiO_2$, and $2Pd–MnO_x/TiO_2$ catalysts

Table 2 Outcomes of deconvolution on Ti 2p and Mn 2p binding energies of the catalysts

Catalyst	Ti^{4+} (% atom)	BE (eV)	Ti^{3+} (% atom)	BE (eV)	Mn^{4+} (% atom)	BE (eV)	Mn^{3+} (% atom)	BE (eV)	Mn^{2+} (% atom)	BE (eV)	Pd^0 (% atom)	Pd^{2+} (% atom)
$2Pd/TiO_2$	100	456.7	0	–	–	–	–	–	–	–	46	54
$6MnO_x/TiO_2$	78	457.4	22	456.2	26	639.5	35	641.7	39	643.2	–	–
$2Pd–MnO_x/TiO_2$	58	459.1	42	456.7	27	639.6	36	641.4	37	643.4	51	49

Ti $2p_{3/2}$:462.8 eV, respectively; this fact indicates that Ti is featured in the Ti^{4+} state, mainly in the Pd/TiO_2 catalyst; in contrast, the $6MnO_x/TiO_2$ and $2Pd–MnO_x/TiO_2$ catalysts disclosed a greater presence of Ti^{3+} species assigned to oxygen vacancies formed through the Mn–O–Ti interaction that provoked an enhanced production of Ti^{3+} by the addition of palladium nanoparticles dispersed in MnO_x/TiO_2, suggesting that the attendance of manganese fostered the formation of vacancies in TiO_2 and this increased with the incorporation of palladium nanoparticles from 14% for $6MnO_x/TiO_2$ to 42% for $2Pd–MnO_x/TiO_2$, severally. Table 2 shows the deconvolution results of titanium 2p and manganese 2p binding energies for the $2Pd/TiO_2$, $6MnO_x/TiO_2$, and $2Pd–MnO_x/TiO_2$ catalysts.

Moreover, the deconvolution for oxygen 1s of the $2Pd/TiO_2$, $6MnO_x/TiO_2$, and $2Pd–MnO_x/TiO_2$ catalysts shows three and four peaks mainly. The first one, at ~ 530.4 eV, is due to lattice oxygen on TiO_2; the second one at ~ 531.3 eV is attributed to OH groups and the third one at ~ 532.5 eV is assigned to the presence of H_2O; [47] an additional peak is related to metal bound oxygen at ~ 528.5 eV, mainly in the $2Pd–MnO_x/TiO_2$ catalyst. Regarding the OH groups, they take relevance in the C_3H_8 and CO oxidation, because they contribute to provide active oxygen species during the reaction, [48] see Table 3.

Referring to manganese 2p spin–orbit doublet peaks in the $6MnO_x/TiO_2$ and $2Pd–MnO_x/TiO_2$ catalysts, the deconvolution was performed to elicit the Mn species. Three peak components were found at ~ 639, ~ 641 and ~ 644 eV, mainly. The peaks at ~ 239 and ~ 641 eV correspond to MnO and Mn_2O_3 species, and the third peak at ~ 644 eV can be assigned to MnO_2 species [49]. It is worth noting that the addition of palladium to the MnO_x/TiO_2 catalyst provoked the appearance of an additional peak at ~ 246 eV related to a satellite peak in the $2Pd–MnO_x/TiO_2$ catalyst. The occurrence of the corresponding satellite peak in the $2Pd–MnO_x/TiO_2$ catalyst demonstrates that palladium in MnO_x/TiO_2 provoked distortion in the TiO_2 lattice owing to atomic disorder in the form of lattice defects, [50] resulting in level changes of oxygen vacancies, see Table 3. Therefore, the XPS study of the $2Pd–MnO_x/TiO_2$ catalysts through deconvolution uncovered the remarkably increase in Ti^{3+} and Mn^{3+} species and abundance of lattice oxygen and OH groups, which may be the species responsible for boosting the catalytic activity for the C_3H_8 and CO oxidation (see Table 1 and the catalytic activity section below).

3.5 Catalyst Surface Interaction with CO Determined by In-Situ DRIFTS

DRIFTS analyses were performed to study the interaction between Pd and Pd–Mn species with a CO probe molecule employing the $2Pd/TiO_2$ and $2Pd–MnO_x/TiO_2$ catalysts, as shown in Fig. 6A and B. The adsorption of CO on the monometallic $2Pd/TiO_2$ catalyst produced two feature bands identified at ~ 2175 and ~ 2079 cm^{-1}; the first one is associated with CO adsorbed on β-Ti^{4+} characteristic of Lewis acid sites from TiO_2 anatase [51] as the band at ~ 2079 cm^{-1} is earmarked to linearly bound CO adsorbed mainly on Pd^0 species. Also, an additional band is observed at ~ 2147 cm^{-1} and is related to CO adsorbed on Pd^{2+} species; [52] when the temperature increases, these bands are observed in a better way at ~ 2154 and ~ 2147 cm^{-1}, indicating the active sites that are present during the carbon monoxide adsorption and oxidation process. Figure 6B presents the CO adsorption at different temperatures for the $Pd–MnO_x/TiO_2$ catalyst; two bands at ~ 2180 and ~ 2154 cm^{-1} were identified; the first one is ascribed to CO adsorbed on Ti^{4+} from the TiO_2 anatase, while the band at ~ 2118 cm^{-1} is ascribed to adsorbed CO linearly bound to Pd^0 species and metallic palladium sites. In addition, the bands at ~ 2044 and ~ 1900 cm^{-1} are characteristic of symmetric and asymmetric vibrations of the di-carbonyl doublet-CO on positively charged palladium atoms and CO adsorption by different palladium and manganese species, named as M-CO in Fig. 6A and B. The band at ~ 2044 cm^{-1} stemmed from CO adsorption on new bimetallic Pd–Mn sites; [52–54] this band appears as the temperature increases from RT to 300 °C, see Fig. 6B.

According to the results, palladium is found in reduced states as Pd^0; likewise, as temperature increases, the oxidized species is present as Pd^{2+} according to the bands located at ~ 2147 cm^{-1}, which correlates well with the XPS results. The data of the $2Pd–MnO_x/TiO_2$ catalyst were entirely different from those of the $2Pd/TiO_2$ monometallic catalyst, where the CO adsorption outcomes suggest that the Pd species are readily oxidized at lower temperatures as observed by the TPR analysis; this information suggests that oxygen can be more reactive by the addition of palladium

Table 3 Outcomes of deconvolution on O 1s binding energies of the catalysts

Catalyst	$O_{I(Ti-O)}$ (% atom)	BE (eV)	$O_{II(O-H)}$ (% atom)	BE (eV)	$O_{III(H2O)}$ (% atom)	BE (eV)	$O_{IV(M-O)}$ (% atom)	BE (eV)
$2Pd/TiO_2$	64	530.2	23	531.2	13	532.3	–	–
$6MnO_x/TiO_2$	60	530.0	30	531.1	10	532.1	–	–
$2Pd–MnO_x/TiO_2$	45	530.0	35	531.0	12	532.2	8	530.4

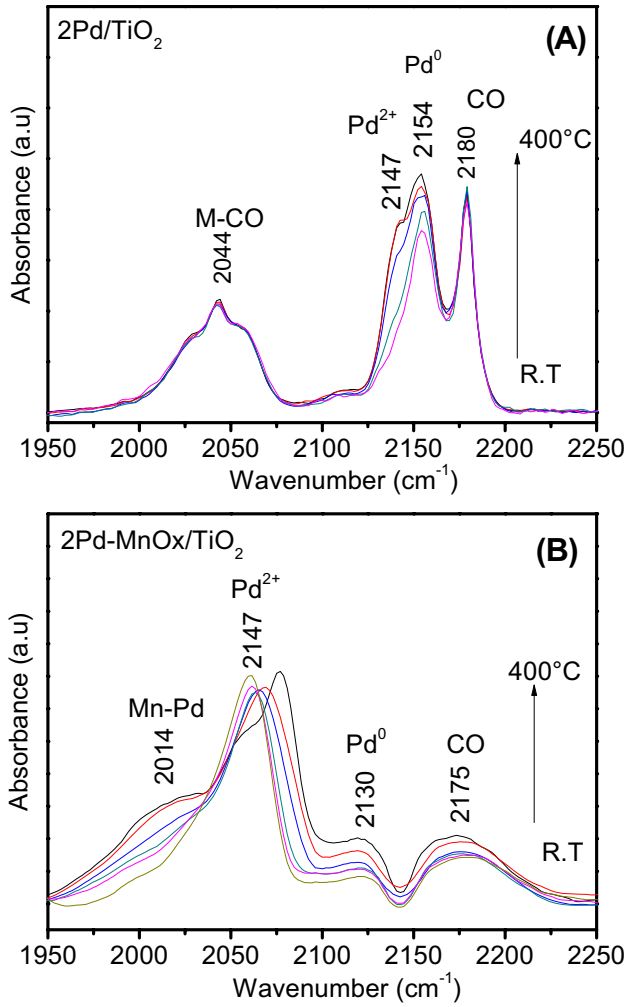

Fig. 6 DRIFTS of the CO adsorption as a function of the temperature for the **A** $2Pd/TiO_2$ and **B** $2Pd–MnO_x/TiO_2$ catalysts

nanoparticles to MnO_x/TiO_2, enhancing the catalytic activity in $2Pd–MnO_x/TiO_2$ with respect to the $2Pd/TiO_2$ catalyst. A promotional effect in the Pd–Mn samples is observed (see catalytic activity section below), providing easy reducibility of Pd^0/Pd^{2+} and Mn^{3+}/Mn^{4+} species, which play an important role in both reactions, propane and CO oxidation to CO_2, which is in agreement with what was observed in [53]. Additional bands located at ~ 2300–2400 cm^{-1} are characteristic of CO_2 intermediate species. On the other hand, several carbon-related species in the frequency region from 1800 to 1200 cm^{-1} were observed in the $2Pd/TiO_2$ and $2Pd–MnO_x/TiO_2$ catalysts. CO_3^{2-} species at ~ 1250–1300 and ~ 1581 cm^{-1}, and mono-dentate carbonate species (CO_3^{2-}) at ~ 1300–1400 cm^{-1} are observed. Whereby, the adsorption bands at 1296 and 1581 cm^{-1} were related to the ν_s(OCO) and ν_{as}(OCO) stretching vibrations of bi-dentate carbonate species (CO_3^{2-}), whereas the band at ~ 1388 cm^{-1} was assigned to the ν_s(OCO) stretching vibration of

mono-dentate carbonate species CO_3^{2-}. The adsorption band at ~ 1248 cm^{-1} was assigned to the presence of asymmetric bicarbonate species (HCO_3^-), which may be formed via the interaction between CO species on Pd nanoparticles and surface hydroxyl groups on the Mn/TiO_2 support, according to earlier literature, see Fig. S1 in the supplementary data and Table 4 [18, 54, 55].

3.6 Catalytic Activity in Propane Oxidation

Figure 7A presents the C_3H_8 conversion as a function of the reaction temperature for TiO_2 synthesized via the sol–gel method. The results from Fig. 7A show that propane oxidation started from 430 °C on the TiO_2-500 catalyst, reaching 100% conversion at 520 °C and was maintained up to 600 °C. The oxidation reaction of propane for the TiO_2-700 catalyst was activated up to 460 °C, reaching 100% conversion at 560 °C. According to these results, only the TiO_2-500 and TiO_2-700 catalysts achieved 100% of propane conversion while the TiO_2-200 catalysts only reached 18% conversion at 600 °C. According to these results, calcination temperatures of the support at 500 °C slightly enhanced the propane conversion.

In this way, in Fig. 7B, the comparison between the different supports and metal catalysts annealed at 500 °C in the oxidation of propane is shown. As expected, the propane conversion is shifted to lower temperatures with the introduction of 1 and 2 wt% of palladium on the MnO_x/TiO_2 catalysts and shows a positive enhancement of the activity and the reaction rate with regard to the $6MnO_x/TiO_2$ and $2Pd/TiO_2$ catalysts, see Fig. 7B and Table 1. So, the catalytic performance is improved by the interaction between Pd–Mn and TiO_2. The introduction of 5 wt% Pd and 10 wt% MnO_x resulted in a decrease in the catalytic C_3H_8 oxidation performance, see supplementary data Fig. S2. It is important to note that all the thermal treatments and presented characterization were performed under air flow due to the better results obtained under air than under hydrogen at 500 °C (Fig. S3), which led us to conclude that the oxidation of C_3H_8 on the $Pd–Mn/TiO_2$ and Pd/TiO_2 catalysts occurred not only on Pd^0 sites but also on Pd^{2+}, improving the oxidation pathway of C_3H_8 under air treatment with respect to hydrogen treatment, where a greater presence of reduced Pd^0 species was observed in agreement with [56].

Table 4 Position of intermediate species obtained by in situ DRIFTS for the $2Pd/TiO_2$, and $2Pd–MnO_x/TiO_2$ catalysts

Catalyst	COO^- (cm^{-1})	HCHO (cm^{-1})	HCO_3^- (cm^{-1})	CO_2 (cm^{-1})
$2Pd/TiO_2$	1650	1510	1320	2300–2400
$2Pd–MnO_x/TiO_2$	1650	1570	1267	2300–2400

A reaction stability test for the $2Pd–MnO_x/TiO_2$ catalysts was carried out at 350 °C for 240 min; as shown in Fig. 7C, the $2Pd–MnO_x/TiO_2$ catalysts achieved above 50% of propane conversion in a dry feed at 350 °C.

3.7 Catalytic Activity in the Carbon Monoxide Oxidation

The CO catalytic oxidation reaction was carried out for the $2Pd/TiO_2$, $6MnO_x/TiO_2$, $1Pd–MnO_x/TiO_2$ and $2Pd–MnO_x/TiO_2$ catalysts annealed at 500 °C, as shown in Fig. 7D. The $6MnO_x/TiO_2$ catalyst got to be active at 150 °C; by increasing the temperature to 220 °C, it reached 100% of CO conversion. Alike, $2Pd/TiO_2$ began to be active at 120 °C, reaching 100% of CO conversion at 180 °C; in contrast, when palladium nanoparticles were added, a forwarding effect was observed on the $1Pd–MnO_x/TiO_2$ and $2Pd–MnO_x/TiO_2$ catalysts, showing activity from 25 °C (CO conversion of 5 and 18%, respectively) and higher reaction rates than the $2Pd/TiO_2$ and $6MnO_x/TiO_2$ catalysts (Table 1). These results suggest that the Pd–Mn species on TiO_2 play an important role enhancing the CO oxidation at 25 °C, where CO molecules were able to be adsorbed and activated on highly dispersed active metal sites such as Pd^0/Pd^{2+} and Mn^{3+}/Mn^{4+} couple species, whereas O_2 molecules could be adsorbed and activated on oxygen vacancies on the TiO_2 surface, where both CO and O species were adsorbed and then transformed into CO_2.

The apparent activation energy values for catalytic conversion of propane behaved as follows: $2Pd–MnO_x/TiO_2$ (76 kJ/mol) < $2Pd/TiO_2$ (90.2 kJ/mol) < $6MnO_x/TiO_2$ (91.4 kJ/mol), see Fig. 7E and for carbon monoxide oxidation it changed as follows: $2Pd–MnO_x/TiO_2$ (42.2 kJ/mol) < $2Pd/TiO_2$ (48.8 kJ/mol) < $6MnO_x/TiO_2$ (49.4 kJ/mol). The apparent activation energy was decreased notably by adding palladium to the $6MnO_x/TiO_2$ material. In fact, a synergistic effect is observed for the combination of Pd and MnO_x in the $1Pd–MnO_x/TiO_2$ and $2Pd–MnO_x/TiO_2$ catalysts in both CO and propane oxidation reactions (Table 1). This phenomenon is consistent with the XPS and TPR characterization, revealing an improvement in the catalytic oxidation capacity of the $2Pd–MnO_x/TiO_2$ catalysts, which confirms the positive effect of adding Pd to MnO_x/TiO_2.

Based on the results of Pd dispersion and reaction rate (Table 1), the turnover frequencies (TOFs) for the $2Pd/TiO_2$ and $2Pd–MnO_x/TiO_2$ catalysts were calculated at 25 °C for CO and at 300 °C for C_3H_8, and the results are summarized in Table 1. The Pd/TiO_2 and $2Pd–MnO_x/TiO_2$ catalysts presented TOFs of 0.010 and 0.077 s^{-1} for the CO oxidation and 4.4×10^{-4} and 8.4×10^{-3} s^{-1} for C_3H_8, respectively. It is clear that the activity was significantly enhanced for the $2Pd–MnO_x/TiO_2$ catalysts, with a TOF 7.7 times higher for CO and 19 times higher for C_3H_8 than those values displayed

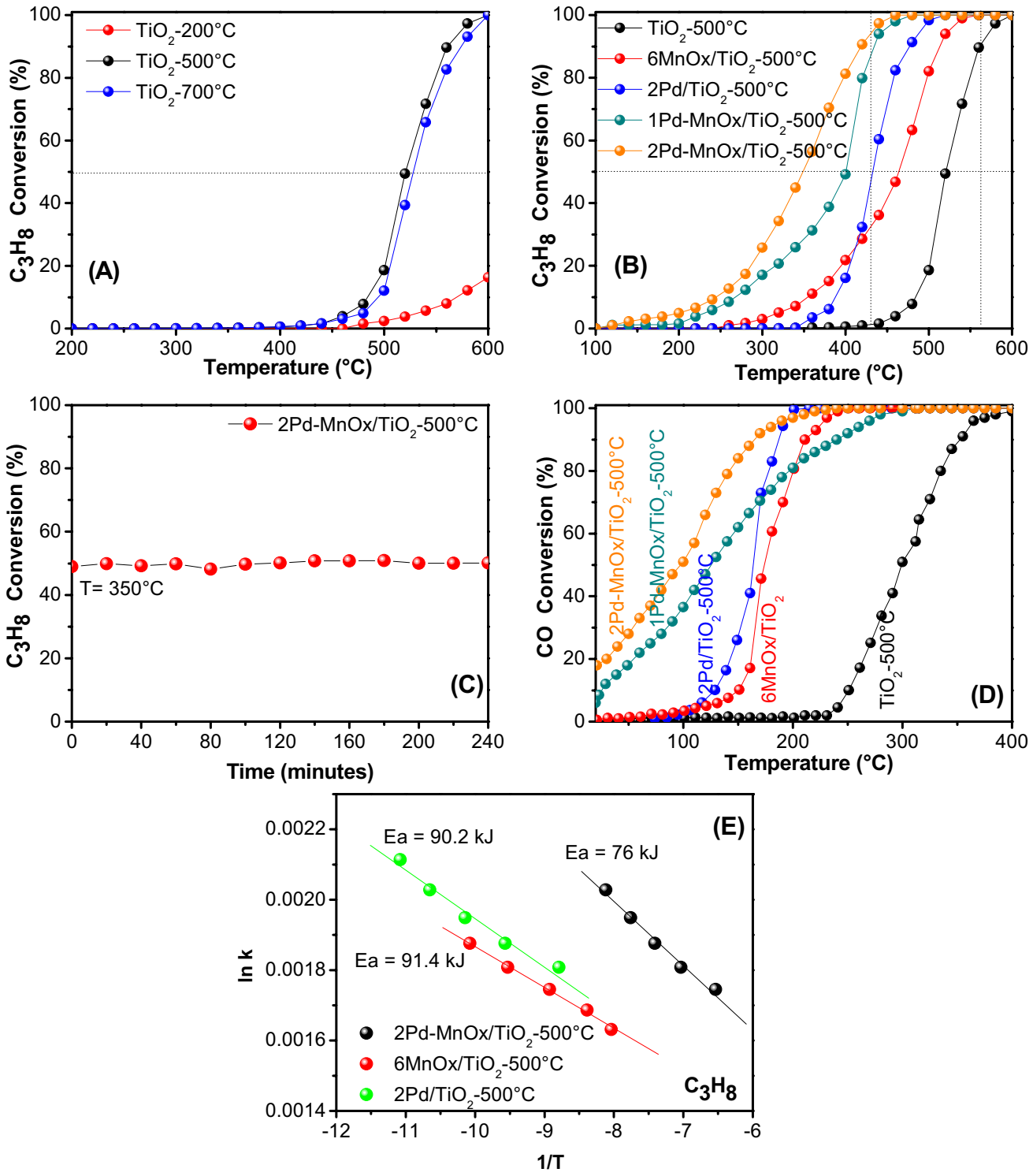

Fig. 7 **A** C_3H_8 conversion for the TiO_2-200, TiO_2-500 and TiO_2-700 catalysts; **B** C_3H_8 conversion for the TiO_2-500 °C, $2Pd/TiO_2$, $6MnO_x/TiO_2$, $1Pd–MnO_x/TiO_2$, and $2Pd–MnO_x/TiO_2$ catalysts; **C** stability test of C_3H_8 conversion for the $2Pd–MnO_x/TiO_2$ catalysts at 350 °C; **D** CO conversion for the TiO_2-500 °C, $2Pd/TiO_2$, $6MnO_x/TiO_2$, $1Pd–MnO_x/TiO_2$ and $2Pd–MnO_x/TiO_2$ catalysts; and **E** Arrhenius plot for the $2Pd/TiO_2$, $6MnO_x/TiO_2$, $2Pd–MnO_x/TiO_2$ catalysts for C_3H_8 oxidation

by the Pd/TiO_2 catalyst. Also, the catalytic performance of the 2Pd–MnO_x/TiO_2 catalyst in the C_3H_8 oxidation was compared with other similar catalysts reported in the literature, see Table 5. As it can be observed in Table 5, the Pd–MnO_x/TiO_2 catalysts here reported show the lowest activation energy values compared with other Pd catalysts supported on pure or mixed oxides that have been previously reported.

The explanation for the best activity observed for the Pd–MnO_x/TiO_2 catalyst in the CO and C_3H_8 oxidation can be given by the characterization results, mainly by the DRIFTS and XPS techniques. The DRIFTS outcomes (Fig. 5) clearly display that Pd^0 and Pd^{2+} were the active species in the oxidation of C_3H_8 and CO by the Pd/TiO_2 catalyst, as previously reported for other catalysts [58]. With regard to the 2Pd–MnO_x/TiO_2 catalyst, the best catalyst in the oxidation of C_3H_8 and CO, it is shown that besides active Pd^0–CO and Pd^{2+}–CO species (2154 and 2147 cm^{-1}), additional active sites at 2014 cm^{-1}, related to Pd–Mn species were produced. These sites could stabilize the interaction between Pd–MnO_x, producing isolated reactive palladium and manganese species sites, which can be related to the species observed by XPS spectroscopy (Pd^{2+}/Pd^0). Thus, these new active sites may explain the enhanced activity in both oxidation reactions by the 2Pd–MnO_x/TiO_2 catalyst with respect to the 2Pd/TiO_2 and 6MnO_x/TiO_2 catalysts.

By analyzing the XPS results (Fig. 5 and Table 3), it is obvious that the 2Pd–MnO_x/TiO_2 catalyst possesses more surface OH groups than the 2Pd/TiO_2 and 6MnO_x/TiO_2 catalysts. Previous studies have reported that surface OH groups are formed by water dissociation on oxygen vacancies, [59] or on metal surfaces through water-oxygen interaction [60]. In this sense, the OH species could facilitate the O_2 adsorption and activation on the TiO_2 support, in agreement with [61] which enhance the diffusion of oxygen along the TiO_2 surface to the metal-support interface, which has been recognized as the active site for oxygen activation [62]. The XPS results also revealed that 2Pd–MnO_x/TiO_2 has a high surface Mn^{3+} content, which induces more surface defect oxygen species. The surface Mn^{3+}/Mn^{4+} and O_{OH}/O_{latt} ratio in the 2Pd–MnO_x/TiO_2 catalyst was enhanced significantly, which may be the key to promoting the catalytic propane performance at lower temperature with respect to the 2Pd/TiO_2 and 6MnO_x/TiO_2 catalysts. These results are consistent with similar works [63], showing that the addition of palladium to the MnO_x/TiO_2 catalyst improved the structural stability of the catalyst, resulting in the enhancing of oxygen vacancies, the surface Mn^{3+}/Mn^{4+} ratio and better oxidation ability. High surface Mn^{3+} concentration will promote the generation of oxygen vacancies, which can take part in propane adsorption, activation and oxidation as shown by the catalytic activity results (Table 1 and Fig. 7). According to previous studies, the oxygen mobility of MnO_x is highly dependent on the transition ability of manganese species ($Mn^{2+} \leftrightarrow Mn^{3+} \leftrightarrow Mn^{4+}$) [64], and when the content of high valence Mn states is risen, the oxygen activity adjacent to the Mn ions would be promoted, as seen by XPS in the 2Pd–MnO_x/TiO_2 catalysts (Fig. 5), which confirmed that this catalyst had a higher oxidation state that promoted oxygen vacancies and higher surface Mn^{3+}/Mn^{4+} ratio, and as consequence, the best oxidation propane ability. Furthermore, the higher surface Mn^{4+} and Mn^{3+} redox couple on the catalyst surface resulted in the high H_2 consumption in H_2/TPR, see (Fig. 4). Therefore, according to these results, it is concluded that palladium plays a significant role in the catalytic oxidation activity by enhancing the formation of oxygen vacancies and active Mn^{3+}/Mn^{4+} couples and by upgrading the surface redox properties compared to the single 6MnO_x/TiO_2 and 2Pd/TiO_2 catalysts, which lacked these characteristics.

To summarize, the presence of Pd led to the formation of Pd–Mn–O, which together improved the production of oxygen vacancies and oxygen mobility with a large amount of Mn^{3+}/$Mn^{4+}$and a higher proportion of Ti^{3+} species. Additionally, the interaction among Pd, MnO_x and TiO_2 enhanced the formation of Ti^{3+} and Mn^{4+}/Mn^{3+} species that are generally accepted as the most active sites for catalytic oxidation over MnO_x-based catalysts [65]. Finally, the promotional effect between Pd nanoparticles on Mn-TiO_2 mixed oxides increased the number of active sites for CO and C_3H_8 oxidation with respect to single 6MnO_x/TiO_2 and 2Pd/TiO_2 catalysts.

Table 5 Comparison of C_3H_8 oxidation catalysts

Catalyst	Ea [kJ]	Temp [°C]	Pd load metal (wt%)	Ref.
Pd/Al_2O_3	132	300–400	0.8	[57]
Pd/TiO_2	95.3	200–400	0.8	[57]
Pd/Mn–Al_2O_3	130.7	200–400	0–8	[57]
Pd/WO_x–TiO_2	121	295–395	2.0	[28]
Pd–MnO_x/TiO_2	76	200–400	2.0	This work

4 Conclusion

Pd–MnO_x/TiO_2 catalysts were synthesized and evaluated for the catalytic oxidation of propane and carbon monoxide. The characterization techniques and catalytic performance revealed the interaction between Pd nanoparticles and MnO_x/TiO_2 on Pd–MnO_x/TiO_2 catalysts. The 2Pd–MnO_x/TiO_2 catalyst exhibited the highest catalytic activity for both C_3H_8 and CO oxidation, achieving 50% of CO and propane conversion at 100 °C and 350 °C, respectively, being active from room temperature for CO oxidation. Promotional effects of palladium in interaction with MnO_x/TiO_2 were confirmed by TPR and XPS

characterizations. Likewise, higher dispersion of palladium promoted the Pd–MnO_x interaction, showing higher proportion of reduced Pd^0 species. The Pd–MnO_x interaction, the Mn^{4+}/Mn^{3+} redox pairs, as well as the presence of abundant oxygen vacancies, enhanced by the reducibility of Ti^{4+} to Ti^{3+}, observed in the Pd–MnO_x/TiO_2 catalysts, may create the active sites for the catalytic oxidation of propane and carbon monoxide over these catalysts, which may explain the higher activity with respect to the $6MnO_x/TiO_2$ and $2Pd/MnO_x$ catalysts.

Supplementary Information The online version contains supplementary material available at https://doi.org/10.1007/s10562-023-04285-3.

Acknowledgements The authors want to thank the financial support provided by the Consejo Nacional de Ciencia y Tecnología (CONACYT) through the CB A1-S-18269 Grant, Dirección General de Asuntos del Personal Académico-UNAM through the PAPIIT IN104022 Grant. We thank Viridiana Maturano for her technical assistance.

Declarations

Conflict of interest The authors declare that they have no conflict of interest.

References

1. Everaert K, Baeyens J (2004) J Hazard Mater 109:113–139
2. Taylor MN, Zhou W, Garcia T, Solsona B, Carley AF, Kiely CJ, Taylor SH (2012) J Catal 285:103–114
3. Solsona B, Aylon E, Murillo R, Mastral AM, Monzonis A, Agouram S, Davies TE, Taylor SH, Garcia T (2011) J Hazard Mater 187:544–552
4. Okal J, Zawadzki M (2011) Appl Catal B 105:182–190
5. Sanz O, Delgado JJ, Navarro P, Arzamendi G, Gandia LM, Montes M (2011) Appl Catal B 110:231–237
6. Rida K, Benabbas A, Bouremmad F, Pen MA, Sastre E, Arias AM (2008) Appl Catal B 84:457–467
7. Zavyalova U, Nigrovski B, Pollok K, Langenhorst F, Muller B, Scholz P, Ondruschka B (2008) Appl Catal B 83:221–228
8. Cheng J, Yu JJ, Wang XP, Li LD, Li JJ, Hao ZP (2008) Ener Fuels 22:2131–2137
9. Milt VG, Ulla MA, Lombardo EA (2000) Catal Lett 65:67–73
10. Armidis MD, Zhang T, Farrauto RJ (1996) Appl Catal B 10:203–227
11. Busca G, Lietti L, Raims G, Berti F (1998) Appl Catal B 18:1–36
12. Wright JD, Sommerdijk NAJM (2001) Sol-gel materials: chemistry and applications. CRC Press, Boca Raton
13. Chen YJ, Dionysiou DD (2006) Appl Catal B 62:255–264
14. Shrestha NK, Yang M, Nah YC, Paramasivam I, Schmuki P (2010) Electrochem Commun 12:254–257
15. Kasuga T, Hiramatsu M, Hoson A, Sekino T, Niihara K (1998) Langmuir 14:3160–3163
16. Bessekhouad Y, Robert D, Weber JV, Chaoui NJ (2004) J Photochem Photobiol A 167:49–57
17. Radojevic M (1998) Environ Pollut S1(102):685–689
18. Peng T, Wang K, He S, Chen X, Dai W, Fu X (2021) Catal Sci Technol 11(6):2261–2272
19. Qian Z, Yunli G, Kaixuan F, Yanfei Z, Qingling L, Chunfeng S, Na J, Degang M (2019) Appl Surf Sci 496:143579
20. Clean Air Technology Center (1999) Technical bulletin: nitrogen oxides (NO_x), why and how they are controlled. US EPA Office of Air Quality Planning and Standards, Research Triangle Park
21. Okal J, Zawadzki M, Tylus W (2011) Appl Catal B 101:548–559
22. Papageorgopoulos D, Keijzer M, Veldhuis J, De Bruijn F (2002) J Electrochem Soc 149:1400–1404
23. Yoshida H, Yazawa Y, Hattori T (2003) Catal Today 87:19–28
24. Descorme C, Taha R, Mouaddib-Moral N, Duprez D (2002) Appl Catal 223:287–299
25. Fang R, Cui Y, Shi Z, Gong M, Chen Y (2015) Chin J Catal 36:994–1000
26. Yi CW, Luo K, Wei T, Goodman DJ (2005) Phys Chem B 109:18535–18540
27. Avila MS, Vignatti CI, Apesteguía CR, Rao VV, Chary K, Garetto TF (2010) Catal Lett 134:118–123
28. García T, Solsona B, Murphy DM, Antcliff KL, Taylor SH (2005) J Catal 229:1–11
29. Yazawa Y, Yoshida H, Komai S, Hattori T (2002) Appl Catal A 233:113–124
30. Todorova S, Naydenov A, Kolev H, Tenchev K, Ivanov Kadinov GG (2007) J Mater Sci 46:7152–7159
31. Puértolas B, Smith A, Vázquez I, Dejoz A, Moragues A, Garcia T, Solsona AB (2013) Chem Eng J 229:547–558
32. Faria WL, Perez CA, César DV, Dieguez LC, Schmal M (2009) Appl Catal B 92:217–224
33. Hanaor DAH, Sorrell CC (2010) J Mater Sci 46:855–874
34. Ettireddy PR, Ettireddy N, Mamedov S, Boolchand P, Smirniotis PG (2007) Appl Catal B 76:123–134
35. Bokhimi X, Morales A, Novaro O, López T, Chimal O, Asomoza M, Gómez R (1997) Chem Mater 9:2616–2620
36. Brunauer S, Deming LS, Deming WE, Teller E (1940) J Am Chem Soc 38:1723–1732
37. Carnö J, Ferradon M, Björnbom E, Järås S (1997) Appl Catal A 155:265–281
38. Chandra Shekar S, Krishna Murthy J, Kanta Rao P, Rama Rao KS (2003) J Mol Catal A 19:45–59
39. Prins R (2012) Chem Rev 112:2714–2738
40. Mendez CM, Olivero H, Damiani DE, Volpe MA (2008) Appl Catal B 84(1–2):156–161
41. Bonarowska M, Pielaszek J, Juszczyk W, Karpinski J (2000) J Catal 195(2):304–315
42. Fagherazzi G, Benedetti A, Polizzi S, Di Mario A, Pinna F, Signoretto M, Pernicone N (1995) Catal Lett 32(3):293–303
43. Li YZ, Xu BL, Fan YN, Feng NY, Qiu AD, He JM, Yan HP, Chen Y (2004) J Mol Catal A 216:107–114
44. Wang CB, Lin HK, Ho CM (2002) J Mol Catal A 180:285–291
45. Huang HB, Leung DYC (2011) ACS Catal 1:348–354
46. Vayenas CG, Bebelis S, Pliangos C, Brosda S, Tsiplakides D (2001) Electrochemical activation of catalysis: promotion, electrochemical promotion, and metal-support interactions. Plenum Press, New York, pp 35–86

47. Sanjinés R, Tang H, Berger H, Gozzo F, Margaritondo G, Lévy F (1994) J Appl Phys 75:2945–2951
48. Schumacher B, Plzak V, Cai J, Behm RJ (2004) Catal Lett 101:215–224
49. Kapteijn F, Vanlangeveld AD, Moulijn JA, Andreini A, Vuurman MA, Turek AM, Jehng JM, Wachs IE (1994) J Catal 150:94–104
50. Wang ZL, Yin JS, Mo WD, Zhang ZJ (1997) J Phys Chem 101:6793
51. Guan H, Lin J, Qiao B, Yang X, Li L, Miao S, Liu J, Wang A, Wang X, Zhang T (2016) Angew Chem Int Ed 55(8):2820–2824
52. Hadjiivanov KI, Vayssilov GN (2002) Adv Catal 47:307–501
53. Wang L, Li G, Wu P, Shen K, Zhang Y, Zhang S, Xiao R (2021) Chem Eng Sci 234:116405
54. Wang K, Jiang R, Peng T, Chen X, Dai W, Fu X (2019) Appl Catal B 256:117780
55. Yue X, Liu X, Wang K, Yang Z, Chen X, Dai W, Fu X (2022) Inorg Chem Front 9(6):1258–1269
56. Camposeco R, Torres AE, Zanella R (2022) Mol Catal 532:112738
57. Gil S, Garcia-Vargas JM, Liotta LF, Pantaleo G, Ousmane M, Retailleau L, Giroir-Fendler A (2015) Catalysts 5(2):671–689
58. Aguirre A, Barrios CE, Aguilar-Tapia A, Zanella R, Baltanás MA, Collins SE (2016) Top Catal 59(2):347–356
59. Zhang Z, Bondarchuk O, Kay BD, White JM, Dohnalek Z (2006) J Phys Chem B 110:21840–21845
60. Vecchietti A, Bonivardi WQ, Xu D, Stacchiola JJ, Calatayud M, Collins SE (2014) ACS Catal 4:2088–2096
61. Ojifinni RA, Froemming NS, Gong J, Pan M, Kim TS, White JM, Henkelman G, Mullins CB (2008) J Am Chem Soc 130:6801–6812
62. Bongiorno A, Landman U (2005) Phys Rev Lett 95:1–4
63. Zhao Q, Ge Y, Fu K, Zheng Y, Liu Q, Song C, Ma D (2019) Appl Surf Sci 496:143579
64. Zhao Q, Liu Q, Han J, Lu S, Su Y, Song C, Ji N, Lu X, Ma D, Cheung OJ (2019) Chem Technol Biotechnol 94(12):3753–3762
65. Liu Z, Zhu J, Li J, Ma L, Woo SI (2014) ACS Appl Mater Interfaces 6:14500–14508